

Sound radiation of 3 MHz driven gas bubbles

Siegfried Grossmann, Sascha Hilgenfeldt, Detlef Lohse

Fachbereich Physik der Universität Marburg, Renthof 6, 35032 Marburg, Germany

Michael Zomack

Schering AG, Clinical Development, Müllerstr. 178, 13342 Berlin, Germany

(November 18, 2018)

The sound radiation of 3 MHz acoustically driven air bubbles in liquid is analysed with respect to possible applications in second harmonic ultrasound diagnostics devices, which have recently come into clinical use. In the forcing pressure amplitude $P_a = 1 - 10$ atm and ambient radius $R_0 = 0.5 - 5 \mu\text{m}$ parameter domain a narrow regime around the resonance radius $R_0 \sim 1 - 1.5 \mu\text{m}$ and relatively modest $P_a \sim 2 - 2.5$ atm is identified in which optimal sound yield in the second harmonic is achieved while maintaining spherical stability of the bubble. For smaller P_a and larger R_0 hardly any sound is radiated; for larger P_a bubbles become unstable towards non-spherical shape oscillations of their surface. The computation of these instabilities is essential for the evaluation of the optimal parameter regime. A region of slightly smaller R_0 and $P_a \sim 1 - 3$ atm is best suited to achieve large ratios of the second harmonic to the fundamental intensity. Spherical stability is guaranteed in the suggested regimes for liquids with an enhanced viscosity compared to water, such as blood.

I. INTRODUCTION

Microbubbles, i.e., gas bubbles of a few μm diameter, have long been known to be very effective scatterers of ultrasound (cf. e.g. [1]). Their scattering cross sections for MHz sound waves can be more than two orders of magnitude greater than their geometrical cross sections [2]. In the last decade, the concept of exploiting this property to perform refined ultrasound diagnostics with gas bubbles as echo contrast enhancers has enjoyed increasing attention [3]. The general idea of this technique is to inject a microbubble suspension into a vein and to study the blood flow by detecting the bubbles' sound echo reaction to an applied acoustical field. This leads to ultrasound images of higher contrast and quality as compared to conventional diagnostic techniques using only the ultrasound backscatter from the tissue itself.

The quality of an ultrasonogram mainly depends on its spatial resolution and its signal intensity, more specifically, on the ratio of signal intensities from “desired” echoes (such as the blood flow in bubble diagnostics) to “background noise” reflections

(from surrounding tissue). Spatial resolution is, of course, limited by the wavelength of the ultrasound. But as the absorption of sound in tissue increases exponentially with frequency [4,5], frequencies below 10 MHz are used in most clinical applications. As a typical value, we will choose an ultrasound driving frequency of $\omega_d/2\pi = 3$ MHz throughout this work.

In doing diagnostics with bubble suspensions, it is desirable to improve the signal to noise ratio. Namely, when detecting the emitted sound from the bubble at the driving frequency 3 MHz, the signal is obscured by the driving and its reflections from tissue. To improve the signal quality, it has recently been proposed [6,7] to detect *higher harmonics* of the driving frequency in the sound emission spectrum of the bubble. In view of the aforementioned strong damping of higher frequencies, the lowest (second) harmonic at 6 MHz is of particular interest. It can be selectively excited if the parameters are chosen appropriately. We expect that soft tissue, driven into the regime of nonlinear response by the strong driving, will also reflect part of the sound in higher harmonics. Also, the large amplitude driving signal itself will undergo nonlinear distortion, generating higher harmonic frequency components [8]. As in the case of the conventional method, it may therefore be necessary to focus on the *difference* between the reflected signal with and without injected microbubbles. However, by choosing the proper size of the bubbles and the proper forcing pressure amplitude, it is possible to enhance the bubbles' reflection signal in higher harmonics. The main focus of this paper is to suggest a parameter regime well suited for such an endeavor.

Experimental and theoretical research on bubble dynamics has received considerable attention since the discovery of single bubble sonoluminescence by Gaitan in 1990 (cf. [9]) and the detailed experiments by the Putterman group at UCLA [10–12]. In those experiments single microbubbles are driven with a frequency of ~ 30 kHz and with a pressure amplitude of $P_a = 1.1 - 1.5$ atm. Under very special conditions on experimental parameters such as the gas concentration in the liquid and the pressure amplitude, the emission of short light pulses (once per driving period) from the center of the bubble is observed. These experiments stimulated us to perform a series of studies on bubble stability [13–18]. Three types of instability mechanisms seem to be important: Spherical instability, diffusive instability, and chemical instability. All of these studies are based on a Rayleigh-Plesset-like (RP) equation which provides an accurate description of the bubble wall dynamics even for strongly nonlinear oscillations. Excellent agreement with the experiments was obtained, encouraging us to rely on the RP equation also for microbubbles driven at 3 MHz. We will give an overview on RP dynamics in section II. Section III shows results of calculated sound intensities emitted into the whole spectrum as well as at the fundamental and second harmonic frequencies. Of the instability mechanisms mentioned above, only shape instabilities are important here. They will be treated in section IV and reveal important restrictions on useful values of driving pressure amplitudes and bubble radii. Section V presents conclusions.

II. RAYLEIGH-PLESSET BUBBLE DYNAMICS

We will treat the dynamics and sound emission of a single bubble here; we assume that it is driven by a spatially homogeneous, standing wave field

$$P(t) = P_a \cos \omega_d t \quad (1)$$

with a frequency $\omega_d/2\pi = 3\text{MHz}$, corresponding to a period of $T = 0.33 \mu\text{s}$, and a sound amplitude P_a between 1 and 10 atm (roughly 10^5 to 10^6Pa), reflecting typical peak pressures of devices in ultrasound diagnostics. Much higher pressure amplitudes, as applied in lithotripters (cf. e.g. [19]), could damage the tissue.

Let us briefly discuss the approximations we made here. In water, the chosen frequency corresponds to a sound wave length of $\lambda = 2\pi c_l/\omega_d \approx 500 \mu\text{m}$, where $c_l = 1481\text{m/s}$ is the sound velocity in water. The typical ambient radius R_0 of the microbubbles is in the range of $1 - 5 \mu\text{m}$. Therefore, the approximation of spatial homogeneity is justified. In diagnostic ultrasound devices, the driving sound is not a standing wave, but a short traveling wave pulse (which is not strictly monochromatic). The corresponding spatial fluctuations of the driving pressure gradient at the location of the bubble will exert translational forces on the bubble. The resulting translational movements of the bubble are neglected (we will come back to this assumption later in this section) as well as bubble-bubble interactions, the so-called secondary Bjerknes forces [20]. Finally, pressure fluctuations due to the blood pressure (order of magnitude 0.05 atm) can also safely be neglected. In many cases, ultrasound contrast enhancers do not contain pure air bubbles, but stabilized bubbles with an albumin or saccharide coating [3]. This may lead to a shift in the resonance frequency of the bubbles as elaborated by de Jong, Church, and others [21–24].

Under these assumptions the dynamics of the bubble radius $R(t)$ may be described by the following ordinary differential equation [25,20]:

$$R\ddot{R} + \frac{3}{2}\dot{R}^2 = \frac{1}{\rho_l} (p(R, t) - P(t) - P_0) + \frac{R}{\rho_l c_l} \frac{d}{dt} (p(R, t) - P(t)) - 4\nu \frac{\dot{R}}{R} - \frac{2\sigma}{\rho_l R}. \quad (2)$$

Typical parameters for an air bubble in water are the surface tension $\sigma = 0.073 \text{kg/s}^2$, the water viscosity $\nu = 10^{-6} \text{m}^2/\text{s}$ and density $\rho_l = 1000 \text{kg/m}^3$. We use these parameters for our calculations. Only the viscosity is chosen to be larger by a factor of three with respect to water ($\nu = 3 \cdot 10^{-6} \text{m}^2/\text{s}$), corresponding to the value for blood. We will later see that the increased viscosity is essential for the spherical stability of the bubble at higher values of P_a . The external (ambient) pressure is $P_0 = 1 \text{atm}$. We assume that the pressure inside the bubble is given by a van der Waals type equation of state

$$p(R(t)) = \left(P_0 + \frac{2\sigma}{R_0} \right) \left(\frac{R_0^3 - h^3}{R^3(t) - h^3} \right)^\kappa \quad (3)$$

with a (collective) van der Waals hard core radius $h = R_0/8.54$ (for air) [26], i.e., h^3 is a measure for the total excluded volume of the molecules. The bubble radius under normal conditions (ambient radius) R_0 is not uniform for the bubble population in a diagnostic suspension. The size distribution can, however, be controlled experimentally and is typically centered around $1\text{--}2\ \mu\text{m}$, with a width of about $1\ \mu\text{m}$ [3]. For the effective polytropic exponent we take $\kappa \approx 1$ as for the oscillation frequencies under consideration micrometer bubbles can be treated as approximately isothermal [27]. Equation (2) can be understood as a balance equation between the excitation due to the forcing (1) on the one hand and dissipative and acoustic loss processes on the other hand.

In this paper, we will denote (2) the (modified) Rayleigh-Plesset (RP) equation, adopting a common practice in recent work on sonoluminescence [28,26,29]. Besides the pioneering work of Lord Rayleigh [25] and Plesset [30], other researchers have contributed to (2) and a number of variations of this equation, e.g. Keller and Miksis [31], Flynn [32], or Gilmore [33]. Some of these variations are much more elaborate than (2). However, a detailed comparison of the solutions obtained from these equations [34,18] shows that significant deviations only occur for bubbles driven at very large pressure amplitudes ($\gtrsim 5\ \text{atm}$) *and* having large radii, i.e., R_0 would have to be substantially larger than for the bubbles of the present study to necessitate the use of a more complicated dynamical equation.

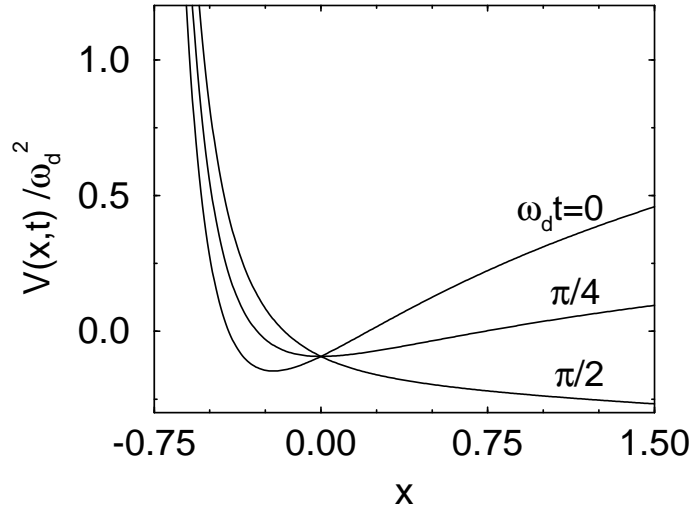


FIG. 1. Potential according to eq. (6), non-dimensionalized through dividing by ω_d^2 , using $P_a = 2\ \text{atm}$ and $R_0 = 1.2\ \mu\text{m}$ for three different phases $\omega_d t = 0, \pi/4, \pi/2$, respectively.

Let us first consider the resonance structure of the RP oscillator in the small forcing limit. To calculate the main resonance frequency we first note that for small forcing $P_a < P_0$ the contribution of the sound coupling to the bubble dynamics (the term $\propto 1/c_l$ on the rhs of equation (2)) is not important. In addition, if R stays large enough to ensure $R^3 \gg h^3$ (which is the case for weak driving), we can replace the van der Waals formula by an ideal gas expression. Writing $R(t) = R_0(1 + x(t))$ we obtain

$$\ddot{x} = \frac{1}{\rho_l R_0^2} \left[\left(P_0 + \frac{2\sigma}{R_0} \right) (1+x)^{-3\kappa-1} - \frac{P_0 + P_a \cos \omega_d t}{1+x} - \frac{2\sigma}{R_0(1+x)^2} \right] - \frac{4\nu \dot{x}}{R_0^2(1+x)} - \frac{3}{2} \frac{\dot{x}^2}{1+x}. \quad (4)$$

We interpret the bracketed term on the rhs of eq. (4) as an effective, time dependent force $-\partial_x V(x, t)$. Integration gives the time dependent potential

$$V(x, t) = \frac{1}{\rho_l R_0^2} \left[\frac{1}{3\kappa} \left(P_0 + \frac{2\sigma}{R_0} \right) (1+x)^{-3\kappa} + (P_0 + P_a \cos \omega_d t) \ln(1+x) - \frac{2\sigma}{R_0} \frac{1}{1+x} \right], \quad (5)$$

which displays a strong asymmetry in x , see Fig. 1. If $P_a = 0$, the equilibrium point is $x = 0$. For general P_a the minimum of the potential oscillates around this value. If $P_a > P_0$ the potential is *repulsive* for a certain fraction of the period. For small P_a and thus small x we can linearize around $x = 0$ and obtain a driven harmonic oscillator

$$\ddot{x} + 2\gamma \dot{x} + \omega_0^2 x = \frac{P_a}{\rho_l R_0^2} \cos \omega_d t \quad (6)$$

with the eigenfrequency

$$\omega_0 = \sqrt{\frac{1}{\rho_l R_0^2} \left(3\kappa P_0 + (3\kappa - 1) \frac{2\sigma}{R_0} \right)} \quad (7)$$

and the damping constant $\gamma = 2\nu/R_0^2$. For fixed driving frequency $\omega_d = 2\pi \cdot 3\text{MHz}$ and $\kappa = 1$ the bubble oscillator is in (main) resonance if $\omega_d = \omega_0$. According to eq. (7), this corresponds to a resonance radius of $R_0 = 1.23 \mu\text{m}$. Taking viscous damping into account, the oscillation amplitude has its maximum value at a frequency [35]

$$\omega_{res}^{(1)} = \sqrt{\omega_0^2 - 2\gamma^2} = \sqrt{\frac{1}{\rho_l R_0^2} \left(3\kappa P_0 + (3\kappa - 1) \frac{2\sigma}{R_0} \right) - \frac{8\nu^2}{R_0^4}}, \quad (8)$$

which (with $\nu = 3 \cdot 10^{-6} \text{m}^2/\text{s}$) shifts the main resonance radius to $R_0^{(1)} = 1.18 \mu\text{m}$. The corresponding radii for the subharmonics $\omega_{res}^{(1/2)} = \omega_d/2$, $\omega_{res}^{(1/3)} = \omega_d/3$, and $\omega_{res}^{(1/4)} = \omega_d/4$ are $R_0^{(1/2)} = 2.18 \mu\text{m}$, $R_0^{(1/3)} = 3.14 \mu\text{m}$, and $R_0^{(1/4)} = 4.09 \mu\text{m}$, respectively. The harmonic $\omega_{res}^{(2)} = 2\omega_d$ is at $R_0^{(2)} = 0.64 \mu\text{m}$. As we will see below, the harmonic and subharmonic resonances will also strongly affect the intensity of the emitted sound.

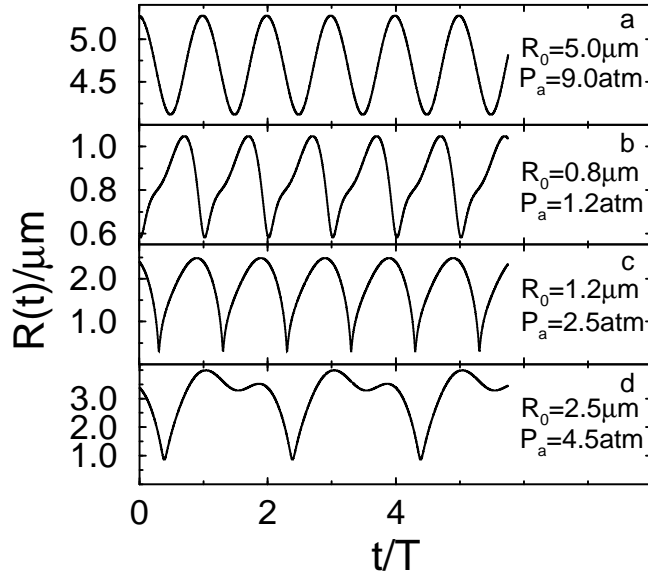


FIG. 2. The bubble radius R vs. time for four different parameter pairs (R_0, P_a) ; from upper to lower: a) $(5 \mu\text{m}, 9.0 \text{ atm})$, b) $(0.8 \mu\text{m}, 1.2 \text{ atm})$, c) $(1.2 \mu\text{m}, 2.5 \text{ atm})$, d) $(2.5 \mu\text{m}, 4.5 \text{ atm})$

Figure 2 shows the time series $R(t)$ for four typical sets of parameters, as computed from (2) and (3) using a double precision, fourth-order, variable stepsize Runge-Kutta algorithm [36]. For small P_a it is trivial that the radius oscillates sinusoidally, but this can also happen for driving pressure amplitudes as large as $P_a = 9 \text{ atm}$, if the radius is much larger than the resonance radius, as seen in figure 2 a). For other parameter combinations, the bubble changes its behavior and exhibits *collapses*, characterized by short duration minima of the radius, accompanied by large accelerations (large curvature of $R(t)$). In figure 2 b) we observe one (weak) bubble collapse per cycle which becomes stronger for larger P_a , see figure 2 c). For strong collapses the typical return time of the collapsing bubble is in the nanosecond range. Like the time series of most nonlinear oscillators, the bubble dynamics can period double so that a collapse only repeats every two cycles, as shown in figure 2 d) for a strong collapse. In other parameter regions, aperiodic behavior (“chaos”) can be observed (cf. [37]). It can also be seen from Fig. 2 that our notion of strong collapse coincides well with Flynn’s [32,38] definition of “transient cavities”, for which the ratio of maximum expansion radius and ambient radius (expansion ratio) must fulfill $R_{max}/R_0 \gtrsim 2$: the examples of Figs. 2 c and d show rapid collapses and an expansion ratio of ~ 2 . On the other hand, Figs. 2 a and b exemplify weakly oscillating bubbles with expansion ratios near one.

For the purposes of this paper, it is instructive to compute the *minimum* radius $R_{min} = \min_t(R(t))$ which the bubble achieves during its oscillation. This quantity is

shown in Fig. 3. For this figure, as for the other 3D plots, the displayed function was evaluated at 100×100 equidistant grid points in the $P_a - R_0$ plane. For weak forcing the minimum radius essentially equals the ambient radius (limit of small oscillations). However, if the driving pressure amplitude is large enough, the bubble collapse is only halted in the immediate vicinity of the smallest possible radius, i.e., the van der Waals hard core radius. The transition towards hitting the hard core radius $h = R_0/8.54$ (upon increasing P_a) is rather abrupt, forming a well-defined threshold in the $P_a - R_0$ plane. Obviously, this transition occurs for smaller P_a if the bubble radius is near one of the above mentioned resonance radii. The resonances at $R_0^{(1)} = 1.18 \mu m$ and $R_0^{(1/2)} = 2.18 \mu m$ are clearly recognized in Fig. 3. As P_a becomes larger, the

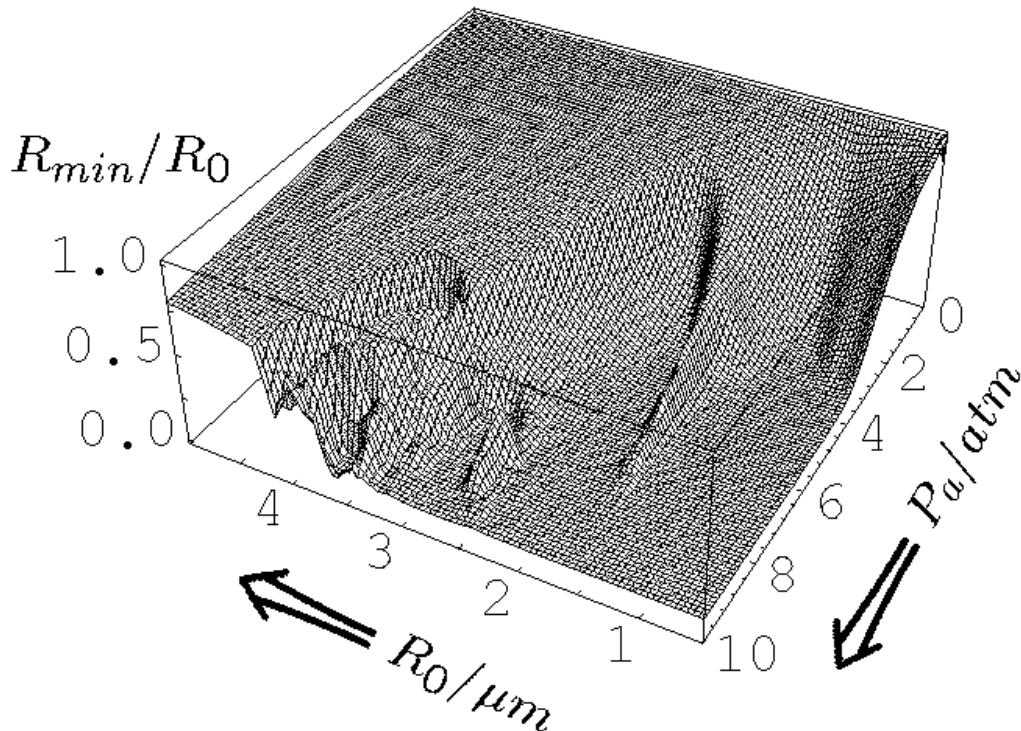


FIG. 3. Minimum radius R_{min}/R_0 as a function of R_0 and P_a . Note that the graph is enclosed between two planes: for small P_a , the quotient R_{min}/R_0 is nearly equal to one (weak oscillations), for large P_a and small R_0 it approaches $h/R_0 = 1/8.54$, with the van der Waals hard core radius h . Arrows in figures 3, 4, 7 – 9 indicate axis orientation.

We now come back to our above assumptions on the pressure field. The results of this work were obtained assuming a driving by standing plane waves. Today's ultrasound diagnostics devices usually emit a bundle of traveling waves that interfere constructively to build up large pressure peaks (5 – 10 atm) and to achieve sufficient spatial resolution. The resulting spatial pressure gradients lead to translational forces acting on the bubble, the so called primary Bjerknes forces [20]:

$$\mathbf{F}_B(\mathbf{r}, t) = V_b(t)\nabla P(\mathbf{r}, t), \quad (9)$$

where $V_b(t)$ is the time dependent volume of the bubble, and $P(\mathbf{r}, t)$ is the external pressure exerted on the bubble. However, numerical computation of (9) shows that the accelerations resulting from a pressure gradient $|\nabla P| \sim P_a/\lambda$ are rather weak and that the translational velocities of the bubbles are small compared to their radial oscillation velocities.

III. SOUND EMISSION OF OSCILLATORY BUBBLES

Our focus of interest is on the sound emitted by the oscillating bubble. The far field sound pressure at a distance $r \gg R$ from the center of the bubble can be calculated as [20,39]

$$P_s(r, t) = \frac{\rho_l}{4\pi r} \frac{d^2 V_b}{dt^2} = \rho_l \frac{R}{r} (2\dot{R}^2 + R\ddot{R}). \quad (10)$$

An ultrasound diagnostics device will display a picture of sound intensity, which is based on the modulus (or, equivalently, the square) of the sound pressure. Obviously, the total detected intensity will not consist exclusively of signals due to (10), but there will also be intensity components from reflections of the incoming signal (1) in the tissue. As these latter contributions depend on many peculiarities of the experimental or diagnostic setup, we do not try to model them here, but focus on the active sound radiation of the bubble.

Figure 4a shows the *total* sound intensity I as a function of the forcing pressure amplitude P_a and the ambient radius R_0 . According to Parseval's theorem it can be calculated either from the sound pressure time series $P_s(r, t)$ or from its Fourier transform $P_s(r, \omega) = \int_0^\tau P_s(r, t) \exp(i\omega t) dt$, $\tau \gg T$, namely

$$I(r) = \frac{1}{\tau} \int_0^\tau |P_s(r, t)|^2 dt = \frac{1}{\tau} \cdot \frac{1}{2\pi} \int_{-\infty}^{+\infty} |P_s(r, \omega)|^2 d\omega. \quad (11)$$

We divide by the length τ of the time series ($\tau \geq 8T$ for all computations) and measure I in units of atm^2 . The intensity is evaluated at a distance of $r_N = 1\text{cm}$ from the bubble's center using standard double precision Fourier transform algorithms [36]. As I spans several orders of magnitude in our parameter regime, we also present its logarithm in Fig. 4 b.

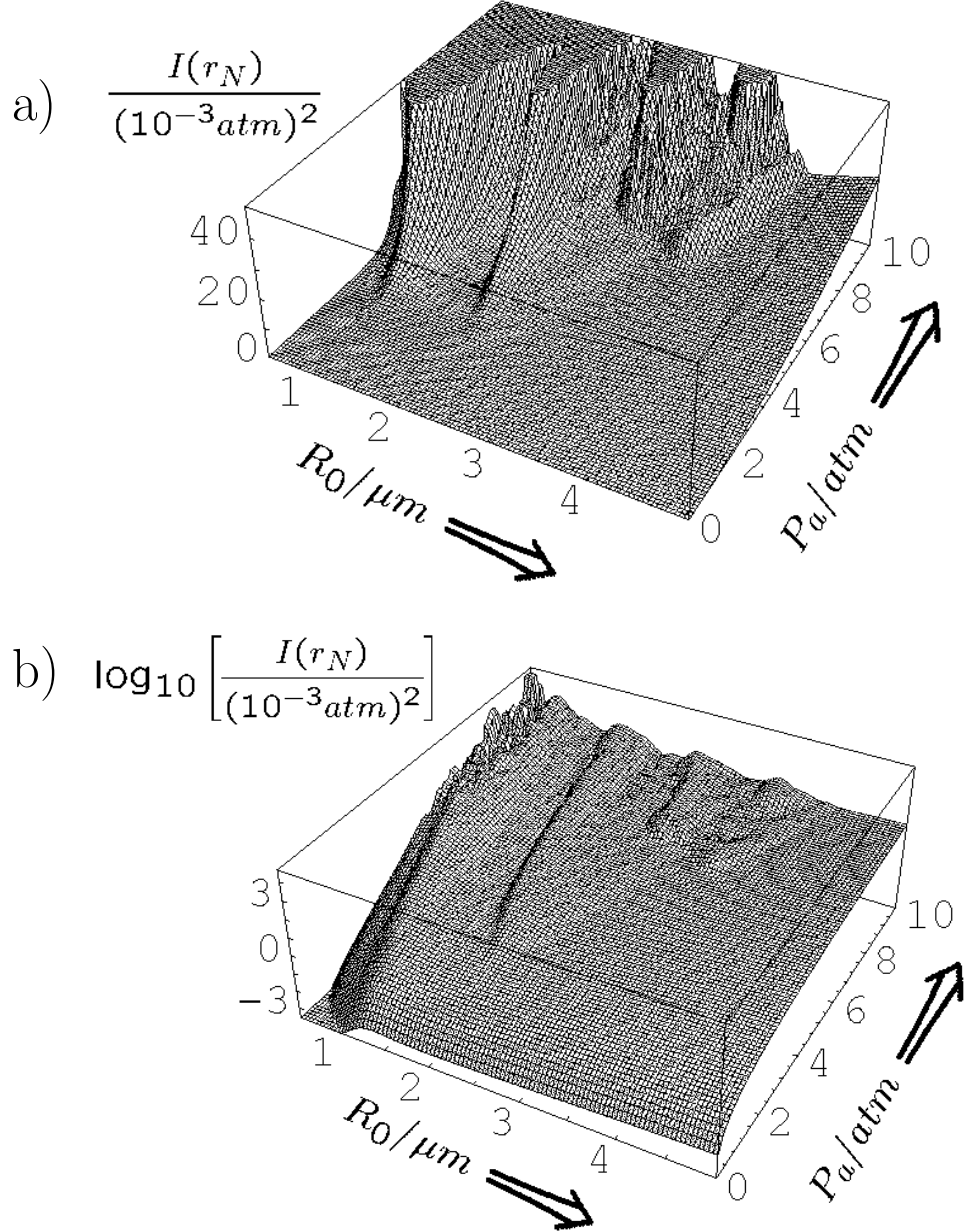


FIG. 4. a) Total sound intensity I at a distance of $r_N = 1\text{cm}$ from the bubble center as a function of R_0 and P_a . The strong correlation between this figure and figure 3 is obvious. Note that the graph is truncated (higher I -values are not displayed) for better illustration of the resonance tongue structure. Figure b) shows a logarithmic plot of the same quantity. The small undulations at very large P_a on top of the resonance structure are due to numerical aliasing in the Fourier analysis and can be reduced with increasing computer power.

It can be seen from Fig. 4 that for small P_a or large R_0 the bubble hardly emits any sound. Sound losses set in at a sharp threshold which is very similar to the threshold seen in Fig. 3 for the minimum radius. Moreover, comparing Figs. 3 and 4 one realizes that strong sound emission and collapsing to the hard core radius are strongly correlated (note the opposite orientations of these two graphs). This behavior is expected from equation (10), as a stronger collapse means larger bubble wall acceleration \ddot{R} at the moment of collapse. The resonance structure in R_0 is also clearly reflected in the emitted sound intensity.

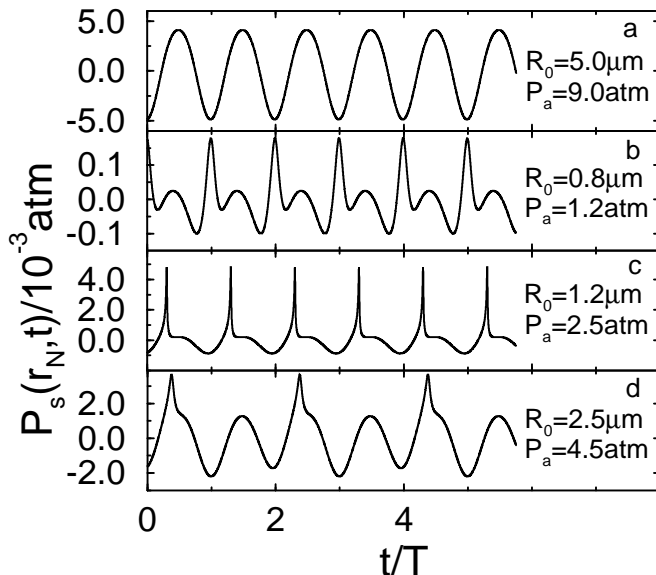


FIG. 5. Time series of the sound pressure $P_s(r_N, t)$ from (10) for the same four pairs of parameters as in figure 2.

Time series of $P_s(r_N, t)$ and their power spectra for the same four parameter pairs (R_0, P_a) as in Fig. 2 are shown in Fig. 5 and Fig. 6, respectively. If the collapse is too violent, the sound intensity is distributed in a broad band spectrum with a large fraction of intensity emitted at higher harmonics, which will be absorbed by the tissue. Therefore it is appropriate to focus on the signal at the second harmonic frequency in order to get high intensities away from the driving frequency. The intensity $I_2(r) = |P(r, \omega = 2\omega_d)|^2 / \tau^2$ in the second harmonic is displayed in Fig. 7. For comparison, we show the same plot also for the intensity $I_1(r) = |P(r, \omega = \omega_d)|^2 / \tau^2$ of the fundamental (driving frequency) in Fig. 8.

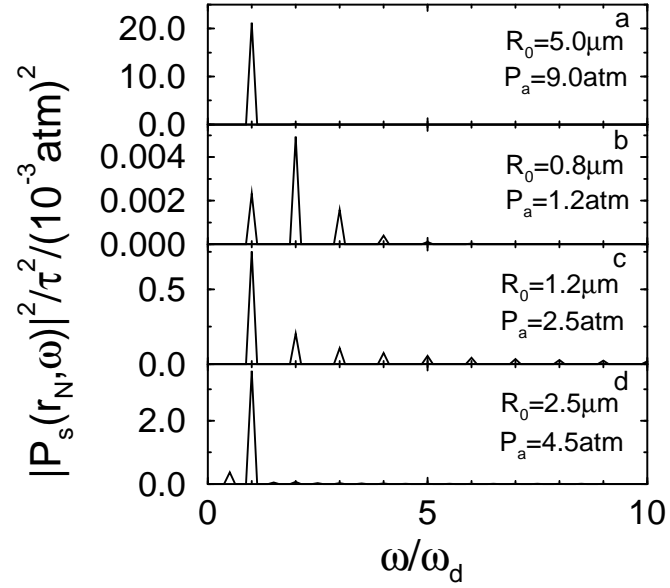


FIG. 6. Power spectra $|P_s(r_N, \omega_d)|^2$ for the same four pairs of parameters as in figure 2.

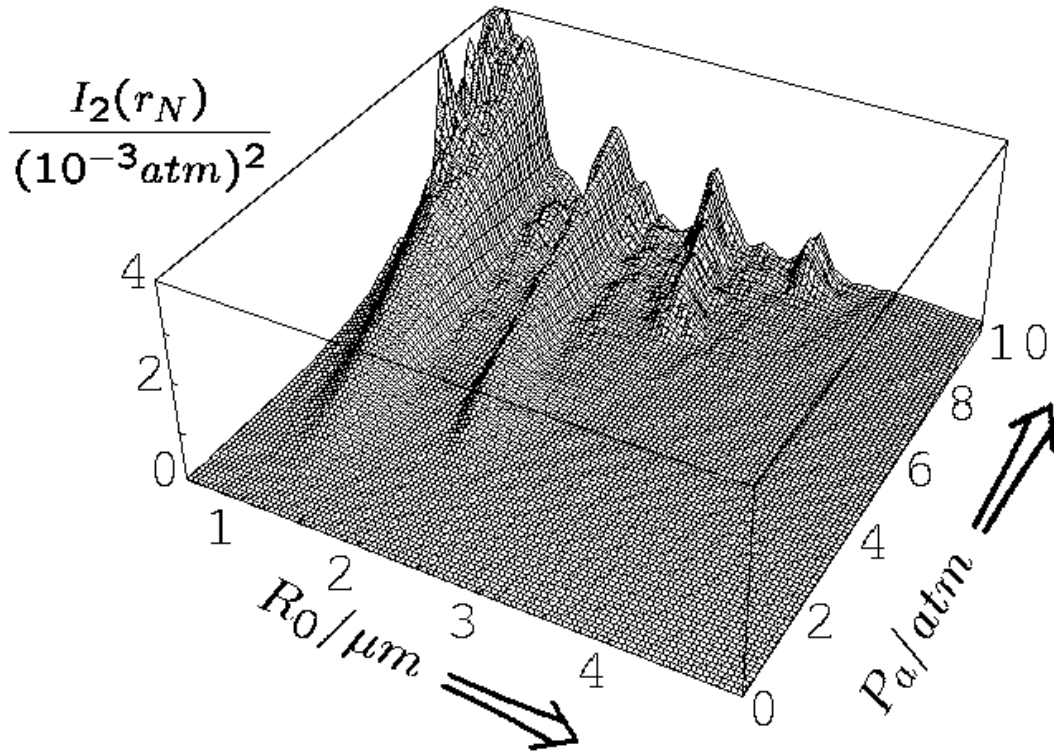


FIG. 7. Absolute intensity of the second harmonic of the sound emission (10).

Not surprisingly, the regions of greatest intensity of the fundamental as well as of the second harmonic coincide with those of the total intensity, i.e., they can be found at the resonance radii. The largest region and the highest maxima of second harmonic intensity occurs around $R_0^{(1)}$. For small P_a the intensity is of course nearly exclusively in the driving frequency itself, which is the frequency of the small oscillations of the bubbles. Upon increasing P_a , sound is also emitted in the second harmonic mode, for some parameter combinations up to 40% of the total intensity. At even larger P_a , higher and higher modes are excited, leaving a smaller and smaller fraction of total intensity for the second mode (cf. Fig. 6 c and d). Even for large P_a , the driving frequency ω_d remains the largest component of total emitted power in spite of the strong collapse, which displays much larger peak pressures, but only lasts for extremely short periods of time.

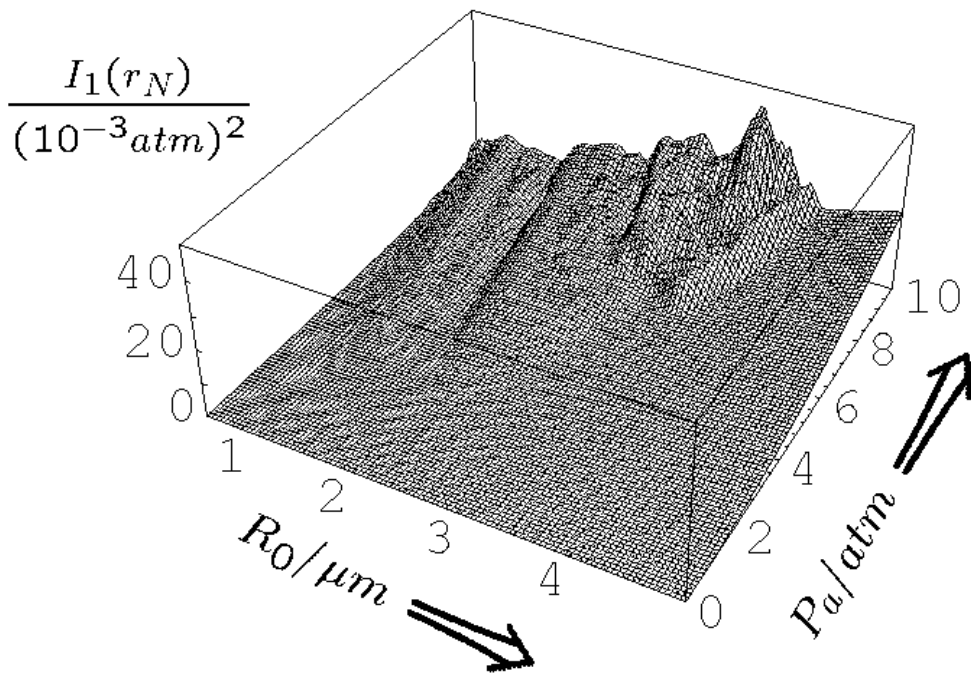


FIG. 8. Absolute intensity of the fundamental of the sound emission (10).

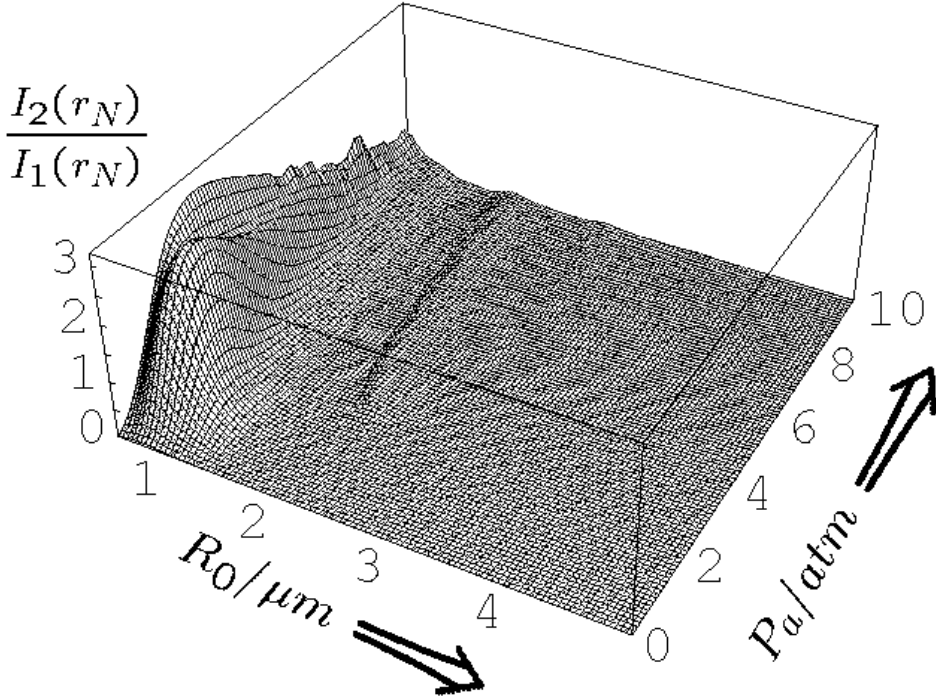


FIG. 9. Ratio I_2/I_1 of intensities of sound emission at the second harmonic and fundamental frequencies.

The key question now is: How should one choose the parameters for optimal detection of the second harmonic? The answer cannot be given exclusively from the absolute intensity of the second harmonic, Fig. 7. Clearly, the signal has to have a certain absolute intensity to overcome the noise level, and therefore Fig. 7 gives important information. One important application of the second harmonic method in ultrasound diagnostics, however, relies on the contrast between intensities at fundamental and second harmonic frequencies: When injecting a bubble suspension into the vascular system, a second harmonic signal is only expected from the contrast agent. Thus, detecting at 6 MHz in our example will give a bright image of the blood vessels. In a diagnostic situation, it should be possible to *switch* between this image and the scattering signal from surrounding tissue, which reflects the 3 MHz driving. But if the bubble emission signal at 3 MHz is more intense than these reflections, the vascular system will be the dominant feature in the fundamental frequency image, too. Therefore, meeting the demands of this application means to identify parameter regions where the *ratio* of second harmonic intensity to fundamental intensity I_2/I_1 is as high as possible. Fig. 9 displays this quantity. It shows a distinct maximum at small $R_0 \approx 0.7 - 0.8 \mu\text{m}$ close to the harmonic bubble resonance radius $R_0^{(2)}$. In this parameter region, the bubble essentially oscillates with 6 MHz instead of 3 MHz; an example for this behavior can be seen in Figs. 5b and 6b. For even smaller radii, a

rise in I_2/I_1 indicates other resonances. All bubbles with high I_2/I_1 ratios emit little absolute acoustic intensity (cf. Figs. 4 – 8).

We have presented a variety of intensity diagrams in Figs. 4 – 9 in order to meet the different demands of different experimental setups or diagnostic applications. Accordingly, the optimal parameter ranges for second harmonic sonography depend on the focus of interest: If the important quantity is relative intensity I_2/I_1 , one would pick the maximum of Fig. 9, i.e., bubbles with $R_0 \approx 0.5 - 1.2 \mu m$ and driving pressure amplitudes $P_a \approx 1 - 3 \text{ atm}$. If absolute intensity is the key variable, one would choose the region around the main resonance radius in R_0 , i.e., $R_0 \approx 1.0 - 1.5 \mu m$. Moreover, Fig. 7 suggests choosing the pressure amplitude P_a as large as possible. However, as we will show in the next paragraph, bubble shape instabilities set an upper limit on practically useful P_a . Note that a change in the driving frequency would shift the resonance radii and, consequently, also the location of regions of maximum sound emission. If, for example, ω_d is smaller, the resonances are shifted towards larger R_0 , see equation (7).

Also, the total amount of bubbles should be large enough to guarantee a strong signal, but low enough to prevent considerable bubble-bubble interaction. Therefore, it is of primary importance to assure that a high percentage of the generated bubbles is in the correct R_0 regime. All other bubbles are essentially useless regarding the yield in the second harmonic and may even obscure the measurements.

IV. SPHERICAL STABILITY

To take advantage of the above suggested parameter regimes derived from RP dynamics, the bubbles in these domains should be *spherically stable*, i.e., stable against the growth of non-spherical bubble deformations, which could eventually lead to bubble fragmentation and a breakdown of sound emission. The corresponding stability analysis has been performed in detail in [15]. We give a brief summary here. Consider a small distortion of the spherical interface $R(t)$,

$$R(t) + a_n(t)Y_n(\theta, \phi),$$

where Y_n is a spherical (surface) harmonic of degree n . An approximate linearized dynamical equation of the distortion $a_n(t)$ for each mode has been derived in [15], following the pioneering work of Prosperetti [40]. It reads (cf. [13])

$$\ddot{a}_n + B_n(t)\dot{a}_n - A_n(t)a_n = 0 \tag{12}$$

with

$$A_n(t) = (n - 1)\frac{\ddot{R}}{R} - \frac{\beta_n\sigma}{\rho_w R^3} - \frac{2\nu\dot{R}}{R^3} \left[(n - 1)(n + 2) + 2n(n + 2)(n - 1)\frac{\delta}{R} \right], \tag{13}$$

$$B_n(t) = \frac{3\dot{R}}{R} + \frac{2\nu}{R^2} \left[(n+2)(2n+1) - 2n(n+2)^2 \frac{\delta}{R} \right]. \quad (14)$$

Here, $\beta_n = (n-1)(n+1)(n+2)$ and δ is a viscous boundary layer cutoff [15],

$$\delta = \min \left(\sqrt{\frac{\nu}{\omega_d}}, \frac{R}{2n} \right). \quad (15)$$

If the coefficients $A_n(t)$ and $B_n(t)$ are periodic with period T , (12) is an equation of Hill's type and instability occurs whenever the magnitude of the maximal eigenvalue of the Floquet transition matrix $F_n(T)$ of eq. (12) is larger than one. The Floquet transition matrix $F_n(T)$ is defined by

$$\begin{pmatrix} a_n(T) \\ \dot{a}_n(T) \end{pmatrix} = F_n(T) \begin{pmatrix} a_n(0) \\ \dot{a}_n(0) \end{pmatrix}. \quad (16)$$

Now for some parameter regimes the radius is not periodic with period T and thus the coefficients $A_n(t)$ and $B_n(t)$ are not either. Therefore, rather than calculating the Floquet matrix $F_n(T)$ we calculate a transition matrix $F_n(NT)$ with a large integer N (here $N = 20$) to average the dynamics. We numerically compute the eigenvalues of $F_n(NT)$. The logarithm of the maximum eigenvalue can be understood as an approximate Lyapunov exponent. If it is positive, the mode $a_n(t)$ grows exponentially and the bubble is unstable towards the corresponding mode of shape oscillation. In Fig. 10 b and 10 c we show the resulting stability diagrams for the second and the third mode ($n = 2$ and $n = 3$, respectively). Bubbles are shape unstable in the dark regions of the $P_a - R_0$ plane, and shape stable in the white areas. Generally, the $n = 2$ mode is the most unstable one, but there are regimes where this does not hold.

The most pronounced features of these stability diagrams are ‘‘tongues’’ of instability. In the low P_a regime equation (12) reduces to a Mathieu equation; in this case the tongues of instability are the well known Mathieu tongues, as demonstrated in [13]. Large viscosity strongly damps out this tongue structure, as seen from comparing the stability diagrams for water and blood (different viscosities) in Fig. 10a and 10b. In some regions of parameter space, stable and unstable points seem to be mixed erratically. This is due to long-periodic or chaotic bubble dynamics for these $P_a - R_0$ combinations, for which the results of our stability analysis over $20T$ depend sensitively on the initial conditions, so that for slightly deviating parameters the stability behavior may be completely different.

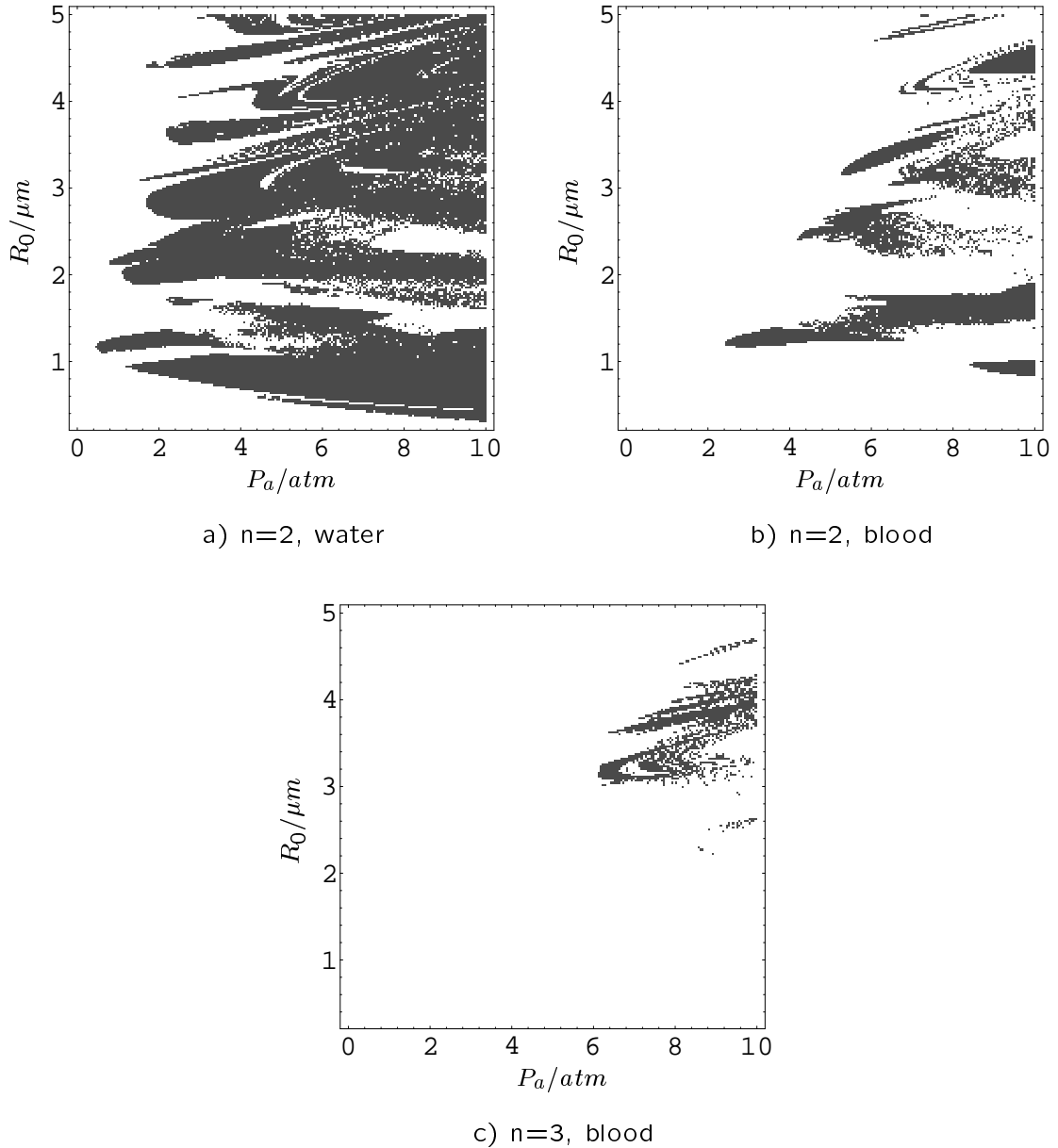


FIG. 10. Stability diagram for the $n = 2$ mode for bubbles in water (a) and in blood (b) and for the $n = 3$ mode for bubbles in blood (c) according to the Floquet multipliers computed from equation (16). In the white regions the bubbles are parametrically stable towards perturbations of the corresponding mode, in the dark regions they are parametrically unstable. Bubbles in water are much less stable than those in blood and higher modes a_n with $n \geq 3$ tend to be more stable than the second mode a_2 . We stress that details of these stability diagrams depend on our approximation (12) – (15) as well as on the choice of the parameters of the liquid and the averaging time which is $20T$ here. Thus they should only be considered as a reflection of the general trend.

As we learn from this figure, bubbles in the R_0 regime of maximum (absolute) yield in the second harmonic become spherically unstable for drivings with $P_a \gtrsim 2.5$ atm. Below, the bubbles are stable in blood (due to its enhanced viscosity), whereas for water these bubbles are unstable with respect to the a_2 -mode even at $P_a \approx 0.5$ atm. Note that it is risky even to be close to an unstable regime, as the bubble may diffusionally shrink or grow into these regimes. This suggests that experiments with bubble suspensions in water will probably give misleading results (with respect to clinical applications) and should rather be carried out in blood or a fluid of correspondingly enhanced viscosity. In our calculations, we have assumed a viscosity of $\nu = 3 \cdot 10^{-6} \text{ m}^2/\text{s}$, which is at the low end of typical measured blood viscosities ($\sim 3 - 5 \cdot 10^{-6} \text{ m}^2/\text{s}$, [41]). Thus, we have determined lower bounds of the instability thresholds in Fig. 10 and the actual regions of stability may be somewhat larger. Note also that stability will be enhanced when lower driving frequencies are used as this leads to a larger effective damping of surface oscillations (cf. [13]).

Stability analysis shows that very large driving amplitudes (say 10 atm) will not help provide large response signals from the suspended bubbles. Instead, it may be useful to limit the amplitudes in the bubble regions to $\lesssim 2.5$ atm.

The predictions for the region of optimal I_2/I_1 intensity ratio remain virtually unaltered, as there is very little overlap of this region with the instability tongues. Indeed, according to the regime of large I_2/I_1 identified above, shape instability in this regime is to be expected only in a tiny area of parameter space at $R_0 \approx 1.2 \mu\text{m}$ and $P_a \approx 3$ atm (see Fig. 10 b).

Besides spherical instability, diffusive instability and chemical instability also are matters of concern, as pointed out in detail for 26 kHz forced bubbles in refs. [15,16]. Both types of instabilities will only be important on long timescales (milliseconds or longer) where our approximation of a stable standing wave is not appropriate anyhow. This is why we postpone the discussion of these instabilities to future work.

V. SUMMARY AND CONCLUSIONS

Bubble suspensions as contrast enhancers in ultrasound diagnostics are now state of the art. Improving the image quality by detecting the second harmonic of the driving frequency in the emitted sound spectrum is likely to lead to their further acceptance, as the advantages compared to conventional methods become even more pronounced. We have identified regions in parameter space, i.e., values for the driving pressure amplitude P_a and the ambient bubble radius R_0 , where relatively high sound intensities at the second harmonic frequency are to be expected. These regions are intimately connected to the resonance structure of the bubble oscillator and to the collapse dynamics of the bubble. The best suited parameter regime to achieve a high absolute second harmonic intensity I_2 is located around the main bubble resonance radius, i.e., $R_0 = 1.0 - 1.5 \mu\text{m}$ if a fixed driving frequency of 3 MHz is used. Requiring

bubble stability towards non-spherical perturbations limits useful driving pressures to a maximum of about 2.5 atm, if the bubbles oscillate in blood (cf. Fig. 10b). Here, we employed the previously specified values for ρ_l , c_l , ν , σ to model the average properties of blood. Bubbles in this parameter range are stable in fluids with (at least) three times higher viscosity than water.

The intensity ratio I_2/I_1 is important for diagnostic purposes (switching between “background” and contrast agent images). It is optimized for bubbles around $R_0 \approx 0.8 \mu\text{m}$ and $P_a \approx 1 - 3 \text{ atm}$. Note that, again, there is an upper limit to the strength of optimal driving.

We therefore suggest not to use very high ($\geq 2.5 \text{ atm}$) pressure amplitudes; a gentler driving may lead to a better image quality. Also, the bubble radii should be somewhat smaller than those dominant in bubble suspensions used today (e.g. SH U 508 A with a radius distribution peak at $\approx 1.4 \mu\text{m}$ [3]), if maximum efficiency at 3 MHz driving frequency is to be achieved. A narrower distribution around the peak (i.e., more uniform radii) would, of course, further amplify the sound signal.

Acknowledgments: The authors thank T. Matula for valuable comments on the manuscript. This work has been supported by the DFG through its SFB185.

-
- [1] R. Gramiak and P. M. Shah, *Invest. Radiol.* **3**, 356 (1968).
 - [2] R. Y. Nishi, *Acustica* **33**, 65 (1975).
 - [3] See the articles in *Advances in echo imaging using contrast enhancement*, edited by N. C. Nanda and R. Schlief (Kluwer Academic Publishers, Dordrecht, 1993).
 - [4] C. M. Sehgal and J. F. Greenleaf, *J. Acoust. Soc. Am.* **72**, 1711 (1982).
 - [5] H. A. H. Jongen, J. M. Thijssen, M. van den Aarssen, and W. A. Verhoef, *J. Acoust. Soc. Am.* **79**, 535 (1986).
 - [6] B. A. Schrope and V. L. Newhouse, *Ultrasound Med. & Biol.* **19**, 567 (1993).
 - [7] P. N. Burns, *Clinical Radiology Suppl.* **51**, 50 (1996).
 - [8] B. Ward, A. C. Baker, and V. F. Humphrey, *J. Acoust. Soc. Am.* **101**, 143 (1997).
 - [9] D. F. Gaitan, L. A. Crum, R. A. Roy, and C. C. Church, *J. Acoust. Soc. Am.* **91**, 3166 (1992).
 - [10] B. P. Barber and S. J. Putterman, *Nature (London)* **352**, 318 (1991).
 - [11] R. Hiller, K. Weninger, S. J. Putterman, and B. P. Barber, *Science* **266**, 248 (1994).
 - [12] For reviews, see L. A. Crum, *Physics Today* **47**, 22 (1994); S. J. Putterman, *Scientific American* **272**, 32 (1995); D. Lohse, *Phys. Blätt.* **51**, 1087 (1995).
 - [13] M.P. Brenner, D. Lohse, and T.F. Dupont, *Phys. Rev. Lett.* **75**, 954 (1995).
 - [14] M.P. Brenner, D. Lohse, D. Oxtoby, and T.F. Dupont, *Phys. Rev. Lett.* **76**, 1158 (1996).
 - [15] S. Hilgenfeldt, D. Lohse, and M. P. Brenner, *Phys. Fluids* **8**, 2808 (1996).
 - [16] D. Lohse, M. Brenner, T. Dupont, S. Hilgenfeldt, and B. Johnston, *Phys. Rev. Lett.* **78**, 1359 (1997); M. P. Brenner, S. Hilgenfeldt, and D. Lohse, “Why air bubbles in water

- glow so easily”, in *Nonlinear Physics of Complex Systems – Current Status and Future Trends*, edited by J. Parisi, S. C. Müller, and W. Zimmermann (Springer Lecture Notes in Physics, Berlin, 1996), p.79.
- [17] M. P. Brenner, S. Hilgenfeldt, D. Lohse and R. Rosales, *Phys. Rev. Lett.* **77**, 3467 (1996).
- [18] S. Hilgenfeldt, M. P. Brenner, S. Grossmann, and D. Lohse, “Analysis of Rayleigh-Plesset dynamics for sonoluminescing bubbles”, submitted to *J. Fluid Mech.* (1997).
- [19] C. C. Church, *J. Acoust. Soc. Am.* **86**, 215 (1989).
- [20] C. E. Brennen, *Cavitation and Bubble Dynamics* (Oxford University Press, Oxford, 1995).
- [21] N. deJong, F. Ten Cate, C. T. Lancee, T. C. Roelandt, and N. Bom, *Ultrasonics* **29**, 324 (1991).
- [22] N. deJong, L. Hoff, T. Skotland, and N. Bom, *Ultrasonics* **30**, 95 (1992).
- [23] C. C. Church, *J. Acoust. Soc. Am.* **97**, 1510 (1995).
- [24] Z. Ye, *J. Acoust. Soc. Am.* **100**, 2011 (1996).
- [25] Lord Rayleigh, *Philos. Mag.* **34**, 94 (1917); M. Plesset, *J. Appl. Mech.* **16**, 277 (1949); W. Lauterborn, *J. Acoust. Soc. Am.* **59**, 283 (1976).
- [26] R. Löfstedt, B. P. Barber, and S. J. Putterman, *Phys. Fluids A* **5**, 2911 (1993).
- [27] M. Plesset and A. Prosperetti, *Ann. Rev. Fluid Mech.* **9**, 145 (1977).
- [28] B. P. Barber and S. J. Putterman, *Phys. Rev. Lett.* **69**, 3839 (1992).
- [29] R. Löfstedt, K. Weninger, S. J. Putterman, and B. P. Barber, *Phys. Rev. E* **51**, 4400 (1995).
- [30] M. Plesset, *J. Appl. Mech.* **16**, 277 (1949).
- [31] J. B. Keller and M.J. Miksis, *J. Acoust. Soc. Am.* **68**, 628 (1980).
- [32] H. G. Flynn, *J. Acoust. Soc. Am.* **58**, 1160 (1975).
- [33] F. R. Gilmore, Hydrodynamics Laboratory, California Institute of Technology, Pasadena, report **26-4** (1952).
- [34] G. J. Lastman and R. A. Wentzell, *J. Acoust. Soc. Am.* **69**, 638 (1981). G. J. Lastman and R. A. Wentzell, *J. Acoust. Soc. Am.* **71**, 835 (1982).
- [35] L. D. Landau and E. M. Lifshitz, *Mechanics* (Pergamon Press, Oxford, 1960).
- [36] W. H. Press, S. A. Teukolsky, W. T. Vetterling, and B. P. Flannery, *Numerical Recipes in FORTRAN* (Cambridge University Press, 1992).
- [37] W. Lauterborn and U. Parlitz, *J. Acoust. Soc. Am.* **84**, 1975 (1988).
- [38] H. G. Flynn and C. C. Church, *J. Acoust. Soc. Am.* **84**, 985 (1988).
- [39] L. D. Landau and E. M. Lifshitz, *Fluid Mechanics* (Pergamon Press, Oxford, 1987).
- [40] A. Prosperetti, *Quart. Appl. Math.* **34**, 339 (1977), see also Ref. [20] and H. W. Strube, *Acustica* **25**, 289 (1971); M. Plesset, *J. Appl. Phys.* **25**, 96 (1954); G. Birkhoff, *Quart. Appl. Math.* **12**, 306 (1954); A. Eller and L.A. Crum, *J. Acoust. Soc. Am. Suppl.* **47**, 762 (1970).
- [41] H. Landolt and R. Börnstein, *Zahlenwerte und Funktionen aus Physik und Chemie* (Springer, Berlin, 1969).